Concurrent multi-peak Bragg coherent x-ray diffraction imaging of 3D nanocrystal lattice displacement via global optimization: Supplementary Information

Siddharth Maddali[1], Travis D. Frazer[1], Nazar Delegan[1,2], Katherine J. Harmon[1], Sean E. Sullivan[1,2], Marc Allain[3], Wonsuk Cha[4], Alan Dibos[5], Ishwor Poudyal[1], Saugat Kandel[4], Youssef S. G. Nashed[6,†], F. Joseph Heremans[1,2,7], Hoydoo You[1], Yue Cao[1,7], and Stephan O. Hruszkewycz[1,*]

[1]Materials Science Division, Argonne National Laboratory Lemont, IL 60439 (USA)
[2]Center for Molecular Engineering, Argonne National Laboratory, Lemont, IL 60439 (USA)
[3]Aix-Marseille Univ, CNRS, Centrale Marseille, Institut Fresnel, Marseille, France
[4]X-ray Science Division, Argonne National Laboratory, Lemont, IL 60439 (USA)
[5]Center for Nanoscale Materials, Argonne National Laboratory, Lemont, IL 60439 (USA)
[6]Mathematics & Computer Science Division, Argonne National Laboratory, Lemont, IL 60439 (USA)
[7]Pritzker School of Molecular Engineering, University of Chicago, 5640 South Ellis Avenue, Chicago, IL 60637 (USA)
[†]Currently at SLAC National Accelerator Laboratory, CA (USA)
[*]Corresponding author: `shrus@anl.gov`

Abstract

Supplementary information for the main manuscript. This document contains:

- Derivation of a mutual orthogonality metric
- Further details and visualization of results.
- Feature preservation with resampling examples.
- Details regarding Fourier transform-based resampling operations utilized within T_i
- Description of constraints of displacement field magnitude

1 Mutual orthogonality

Here, we define the metric of mutual orthogonality used to determine the suitability of using different potential axes of rotation of the sample during a rocking curve.

Consider a 3×3 matrix $\boldsymbol{M} \equiv [\boldsymbol{v}_1\ \boldsymbol{v}_2\ \boldsymbol{v}_3]$ whose columns represent 3 linearly independent vectors spanning 3D Euclidean space $\mathbb{R}^3$. Here each of the $\boldsymbol{v}_i \in \mathbb{R}^3$ is a 3×1 column vector. The *mutual orthogonality* (MO) of $\boldsymbol{M}$ is defined as:

$$\mathcal{O}(\boldsymbol{M}) \equiv \frac{\boldsymbol{v}_1 \cdot \boldsymbol{v}_2 \times \boldsymbol{v}_3}{\|\boldsymbol{v}_1\| \, \|\boldsymbol{v}_2\| \, \|\boldsymbol{v}_3\|} \tag{1}$$

$$= \frac{\det(\boldsymbol{M})}{\|\boldsymbol{v}_1\| \, \|\boldsymbol{v}_2\| \, \|\boldsymbol{v}_3\|} \tag{2}$$

Here $\|\cdot\|$ denotes the Euclidean distance or the L_2-norm. We see that $\mathcal{O}(\boldsymbol{M})$ is invariant under even permutations of the $\boldsymbol{v}_i$'s and changes sign but not magnitude under odd permutations. This follows simply from the same properties of the determinant $\det(\boldsymbol{M})$. A positive (negative) sign of $\mathcal{O}(\boldsymbol{M})$ indicates that the columns of $\boldsymbol{M}$ are right (left) -handed in order.

If the basis vectors are mutually orthogonal (*i.e.*, $\boldsymbol{v}_1 \perp \boldsymbol{v}_2 \perp \boldsymbol{v}_3$), then we see that $\mathcal{O}(\boldsymbol{M}) = \pm 1$, indicating a rectangular basis for $\mathbb{R}^3$. If they all lie in the same plane, $\mathcal{O}(\boldsymbol{M}) = 0$ and the 'basis' does not in fact span $\mathbb{R}^3$. Thus,

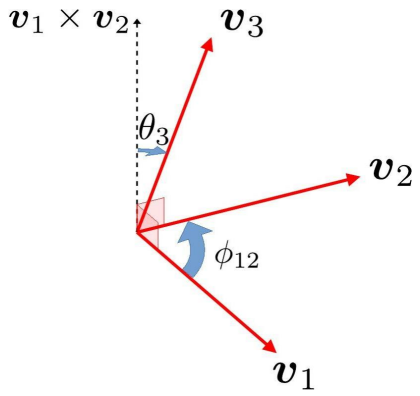

Supplementary Figure 1: Schematic elucidating angle parameterization of MO for a basis matrix $\boldsymbol{M} = [\boldsymbol{v}_1\ \boldsymbol{v}_2\ \boldsymbol{v}_3]$.

$\mathcal{O}(\boldsymbol{M}) \in [-1, 1]$ contains information about the relative independence of the basis vectors of $\boldsymbol{M}$, as well as their handedness.

We refer to Supplementary Figure 1. Here, $\mathcal{O}(\boldsymbol{M})$ can be parameterized in terms of the angles between different vectors from the magnitudes of the cross and dot products:

$$\mathcal{O}(\boldsymbol{M}) = \frac{\|\boldsymbol{v}_3\|\,\|\boldsymbol{v}_1 \times \boldsymbol{v}_2\| \cos\theta_3}{\|\boldsymbol{v}_1\|\,\|\boldsymbol{v}_2\|\,\|\boldsymbol{v}_3\|} \tag{3}$$

$$= \frac{\|\boldsymbol{v}_3\|\,(\|\boldsymbol{v}_1\|\,\|\boldsymbol{v}_2\| \sin\phi_{12}) \cos\theta_3}{\|\boldsymbol{v}_1\|\,\|\boldsymbol{v}_2\|\,\|\boldsymbol{v}_3\|} \tag{4}$$

$$= \sin\phi_{12} \cos\theta_3 \tag{5}$$

We see that the MO of a basis of vectors does not depend on their magnitudes, but only their relative orientations. This parameterization is useful in determining the relation between the orthogonalities of mutually Fourier-conjugate bases, as we see below.

The formulation of MO as given above is particularly useful in BCDI. The measurement consists of rectilinear (but not orthogonal) samples of x-ray intensity in reciprocal (Fourier) space, given by a 3×3 sampling basis matrix $\boldsymbol{B}_{\text{recip}}$ [1, 2]. In other words, Fourier space is sampled at points $\boldsymbol{q}$ obtained from integer combinations of the basis vectors.

$$\boldsymbol{q} = l\boldsymbol{v}_1 + m\boldsymbol{v}_2 + n\boldsymbol{v}_3 \tag{6}$$

$$= \boldsymbol{B}_{\text{recip}} \begin{bmatrix} l \\ m \\ n \end{bmatrix} \tag{7}$$

where $l, m, n \in \mathbb{Z}$.

In practice, the integers l, m, n range over N_1, N_2, N_3 values respectively: $l = 0, 1, \ldots, N_1 - 1$, and so on for m and n as well. Thus, the Fourier window is of size $N_1 \times N_2 \times N_3$ pixels.

The columns of $\boldsymbol{B}_{\text{recip}}$ are determined by the diffraction geometry and the chosen manner of crystal rotation ('rocking'). This in turn unambiguously determines the conjugate basis $\boldsymbol{B}_{\text{real}}$ whose columns denote the real-space samplings steps of the object wave (*i.e.*, the object itself). The real-space object sampled using $\boldsymbol{B}_{\text{real}}$ is related to the propagated wave sampled in the far field using $\boldsymbol{B}_{\text{recip}}$ through the discrete Fourier transform. The relation between the conjugate bases is given by [1]:

$$\boldsymbol{B}_{\text{real}} = \boldsymbol{B}_{\text{recip}}^{-T} \underbrace{\begin{bmatrix} N_1 & & \\ & N_2 & \\ & & N_3 \end{bmatrix}^{-1}}_{\mathcal{D}=\text{diag}(N_1,N_2,N_3)} \tag{8}$$

where we have denoted $\mathcal{D} \equiv \text{diag}(N_1, N_2, N_3)$. Here, $(\cdot)^{-T}$ equivalently denotes the inverse of the transpose or the transpose of the inverse. As we can see, a larger Fourier window (greater N_1, N_2, N_3) results in a better real-space resolution *limit* (smaller sampling steps).

The rotating crystal geometry in BCDI ensures that the diffraction signal is always sampled not in a well-behaved, rectangular manner, but with a linear shear. In other words, $\|\mathcal{O}(\boldsymbol{B}_{\text{recip}})\| < 1$. This naturally introduces a shear into the real-space sampling basis $\boldsymbol{B}_{\text{real}}$ through Supplementary Equation (8). In the light of this, we would like

to determine the relation between $\mathcal{O}(\boldsymbol{B}_{\text{recip}})$ and $\mathcal{O}(\boldsymbol{B}_{\text{real}})$. Ideally, we would prefer $\mathcal{O}(\boldsymbol{B}_{\text{recip}})$ for each scan in a multi-reflection BCDI measurement to be as close to unity as possible, and therefore one must arrange their measurements accordingly. In our simulations, we choose to exercise this flexibility rather coarsely through one of two rocking directions, namely θ and ϕ from Figure 1 in the main text. These correspond to motor stages at the 34-ID-C coherent diffraction instrument at the Advanced Photon Source.

We seek an expression for $\mathcal{O}(\boldsymbol{B}_{\text{real}})$ in terms of $\mathcal{O}(\boldsymbol{B}_{\text{recip}})$. In order to do this, we first define $\boldsymbol{\beta}_{\text{recip}} \equiv \boldsymbol{B}_{\text{recip}}\mathcal{D}^{1/2}$ and $\boldsymbol{\beta}_{\text{real}} \equiv \boldsymbol{B}_{\text{real}}\mathcal{D}^{1/2}$. This implies that Supplementary Equation (8) can be rewritten more simply as:

$$\boldsymbol{\beta}_{\text{real}}^{T}\boldsymbol{\beta}_{\text{recip}} = \mathbb{1} \tag{9}$$

where $\mathbb{1}$ is the 3×3 identity matrix. From the above definitions, we see that $\boldsymbol{B}_{\text{real}}$ ($\boldsymbol{B}_{\text{recip}}$) differs from $\boldsymbol{\beta}_{\text{real}}$ ($\boldsymbol{\beta}_{\text{recip}}$) only in the magnitudes of the columns, and therefore we have: $\mathcal{O}(\boldsymbol{\beta}_{\text{recip}}) = \mathcal{O}(\boldsymbol{B}_{\text{recip}})$ and $\mathcal{O}(\boldsymbol{\beta}_{\text{real}}) = \mathcal{O}(\boldsymbol{B}_{\text{real}})$. It is therefore sufficient to determine the relation between $\mathcal{O}(\boldsymbol{\beta}_{\text{recip}})$ and $\mathcal{O}(\boldsymbol{\beta}_{\text{real}})$.

If $\boldsymbol{\beta}_{\text{recip}} \equiv [\boldsymbol{k}_1\ \boldsymbol{k}_2\ \boldsymbol{k}_3]$ and $\boldsymbol{\beta}_{\text{real}} \equiv [\boldsymbol{r}_1\ \boldsymbol{r}_2\ \boldsymbol{r}_3]$, then Supplementary Equation (9) tells us that:

$$\boldsymbol{r}_l = \frac{\epsilon_{lmn}\boldsymbol{k}_m \times \boldsymbol{k}_n}{\det(\boldsymbol{\beta}_{\text{recip}})} = \frac{\epsilon_{lmn}\boldsymbol{k}_m \times \boldsymbol{k}_n}{\boldsymbol{k}_1 \cdot \boldsymbol{k}_2 \times \boldsymbol{k}_3} \text{ for } l, m, n = 1, 2, 3 \tag{10}$$

$$\implies \|\boldsymbol{r}_l\| = \frac{1}{\|\boldsymbol{k}_l\| \cos\theta_l} \qquad \text{(from the geometry in Supplementary Figure 1)}$$

Here ϵ_{lmn} is the Levi-Civita symbol denoting the cyclic relation between the indices l, m and n. We therefore have:

$$\mathcal{O}(\boldsymbol{\beta}_{\text{real}}) = \frac{\det(\boldsymbol{\beta}_{\text{real}})}{\|\boldsymbol{r}_1\|\,\|\boldsymbol{r}_2\|\,\|\boldsymbol{r}_3\|} \tag{11}$$

$$= \frac{\|\boldsymbol{k}_1\|\,\|\boldsymbol{k}_2\|\,\|\boldsymbol{k}_3\|}{\det(\boldsymbol{\beta}_{\text{recip}})} \cos\theta_1 \cos\theta_2 \cos\theta_3 \qquad (\because \det\boldsymbol{\beta}_{\text{real}} = 1/(\det\boldsymbol{\beta}_{\text{recip}}) \text{ from Supplementary Equation (9)})$$

$$\implies \boxed{\mathcal{O}(\boldsymbol{\beta}_{\text{real}}) = \frac{\cos\theta_1 \cos\theta_2 \cos\theta_3}{\mathcal{O}(\boldsymbol{\beta}_{\text{recip}})}} \tag{12}$$

We note that a high MO in reciprocal space indicates a similarly high MO in real space. These MOs respectively pertain to how the signal and the scatterer are discretized. Hence choosing $\mathcal{O}(\boldsymbol{B}_{\text{recip}})$ as close to 1 as possible by judicious choice of crystal rotation (in particular, rocking about the θ or ϕ axis) facilitates the best orthogonal discretization of the reconstructed object wave, owing to interpolation from a minimally sheared sampling basis $\boldsymbol{B}_{\text{real}}$.

2 Further details and visualization of results

Supplementary Figure 2 shows the results of individual phase retrieval reconstructions of the 5 BCDI scans simulated for the simulated dislocation-free crystal (object wave amplitude). Each row in Supplementary Figure 2(a) corresponds to the central slice along the $i-j$, $k-i$ and $j-k$ planes of the 3D array space of the final reconstructions ψ_{ijk}. These slices are in general not orthogonal, since the real-space sampling directions encoded in each $\boldsymbol{B}_{\text{real}}$ are not orthogonal. The phase retrieval was performed with the open-source Python module Phaser [3]. The phase retrieval recipe chosen was a combination of ER, HIO and SF (solvent flipping) with intermittent shrinkwrap-based update of the object support. Each reconstruction took 0.5 seconds with an Nvidia Tesla P100 GPU. An error function fit to the line profile in 2(b) is shown in 2(c), with an estimated spatial resolution of 39.8 nm. The exact phase retrieval recipe used for reconstruction was as follows:

1. 150 iterations of ER, with shrinkwrap every 30 iterations.
2. 300 iterations of HIO.
3. 100 iterations of solvent-flipping (SF), with shrinkwrap every 25 iterations.
4. 300 iterations of HIO.
5. 450 iterations of ER, with shrinkwrap every 90 iterations.

All these algorithms are reviewed in Ref. [4].

Similarly, Supplementary Figure 3 shows the single Bragg peak phase retrieval results for the simulated data from the crystal containing dislocations. The uniformity of amplitude is notably worse than in the case of the coupled MR-BCDI reconstruction presented in the main text. Supplementary Figure 4(a) shows the final loss function value of $\mathcal{L}_{\text{multi}} \sim 1$ and histograms of residuals for the MR-BCDI reconstruction of the simulated crystal containing a dislocation.

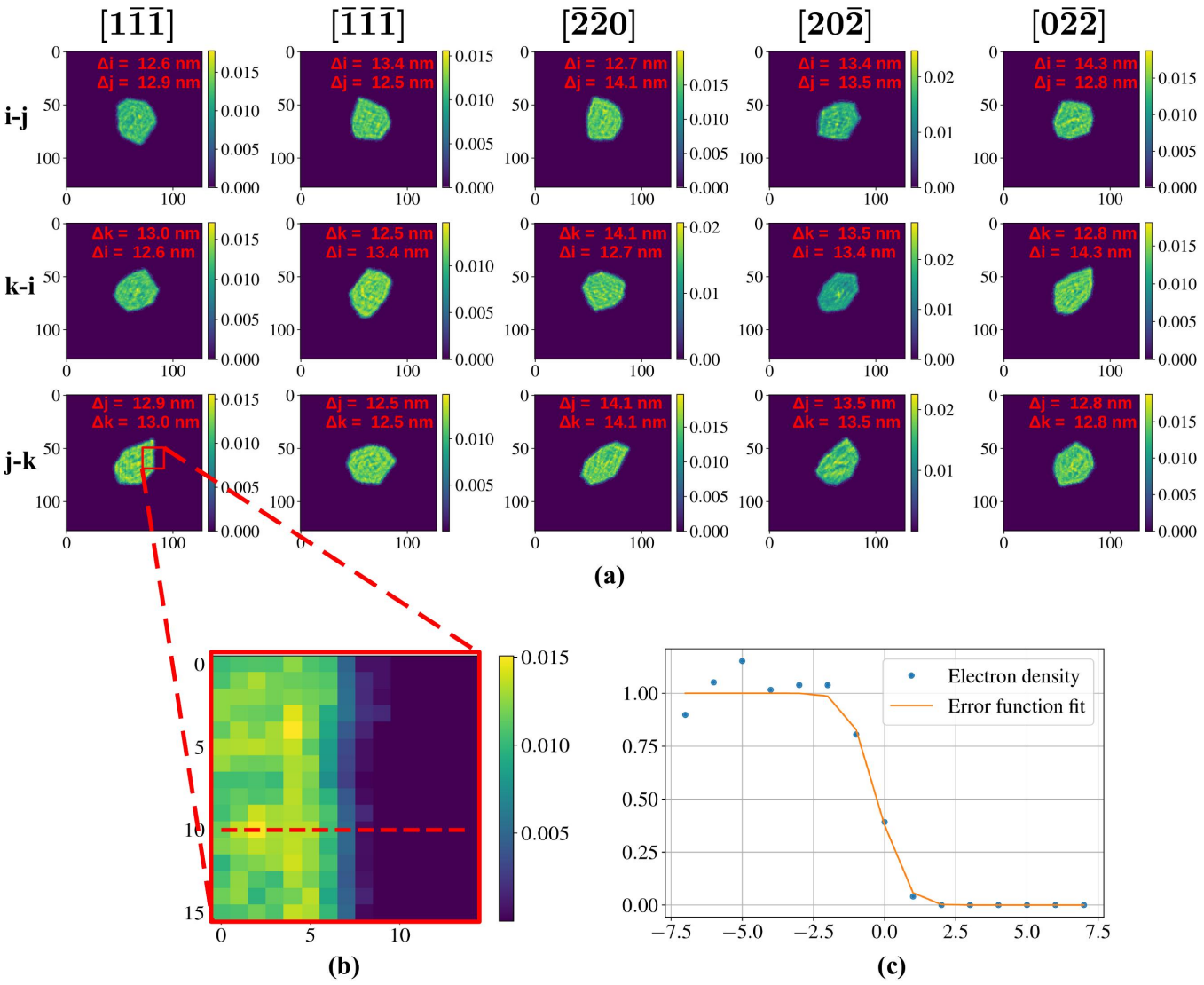

Supplementary Figure 2: **(a)** Phase retrieval reconstructions of the object wave amplitudes ($\left\|\psi^{(i)}\right\|$), corresponding to the 5 individual BCDI scans from the dislocation-free crystal. The voxel sizes in nanometers are the magnitudes of the columns of the corresponding $\boldsymbol{B}^{(i)}_{\text{real}}$ matrix. We note that these basis vectors are not orthogonal in general, and therefore the slices shown in each column do not correspond to orthogonal slices. **(b)** Magnified view of one of the reconstructions, with a line profile extracted along the dashed line. **(c)** Error function fit to the line profile in (b), with an estimated spatial resolution of $1.3\sqrt{8\ln 2} = 3.06$ pixels, or $1.3\sqrt{8\ln 2} \times 13 = 39.8$ nm. The multiplier of 13 comes for the Δk pixel pitch in the corresponding image in (a).

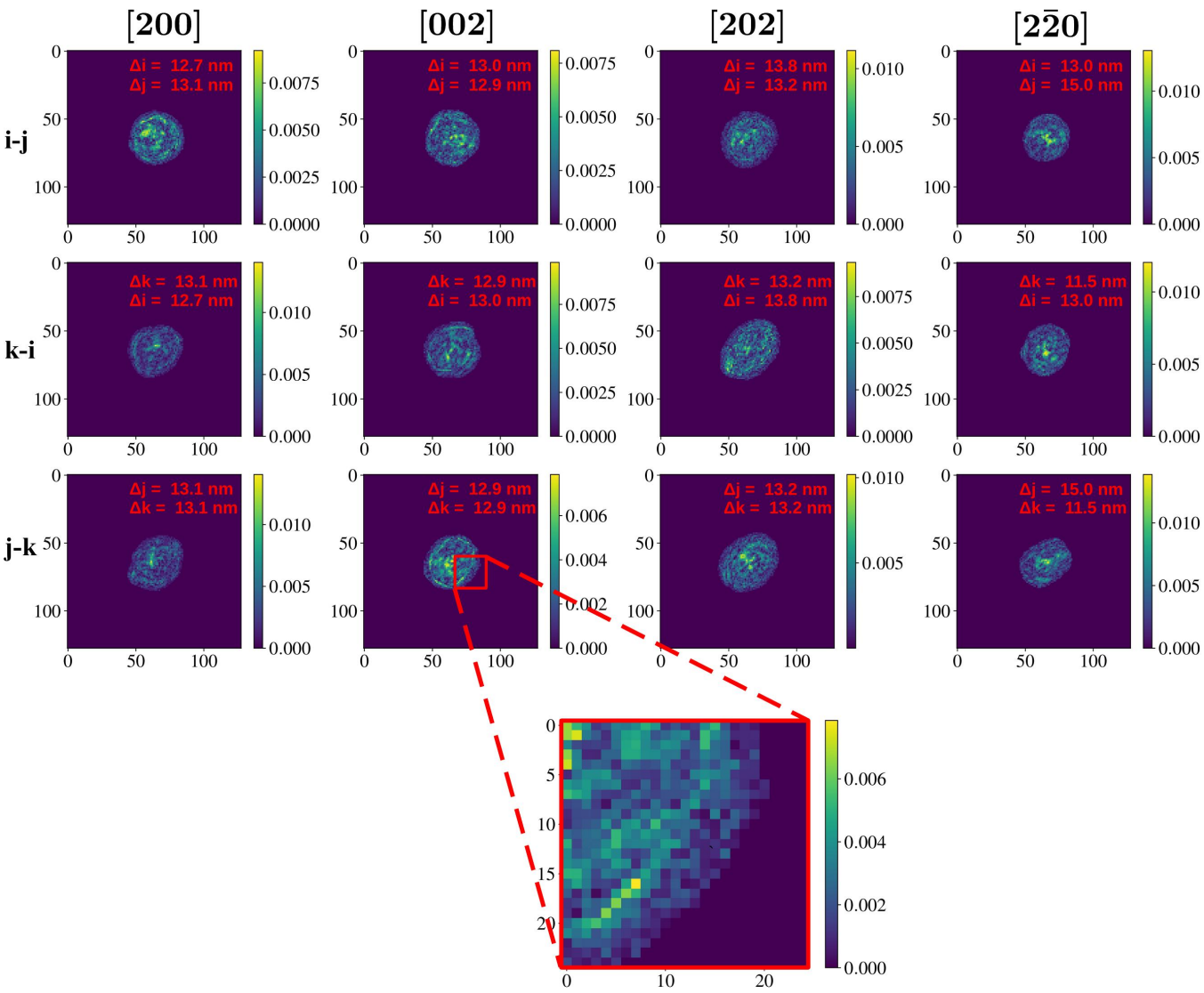

Supplementary Figure 3: **(a)** Individual amplitude reconstructions $\left\|\psi^{(i)}\right\|$ from phase retrieval applied to the BCDI scan the crystal with screw dislocations (complex amplitude), using the recipe above. The cross sections shown correspond to the same slices in Supplementary Figure 2.

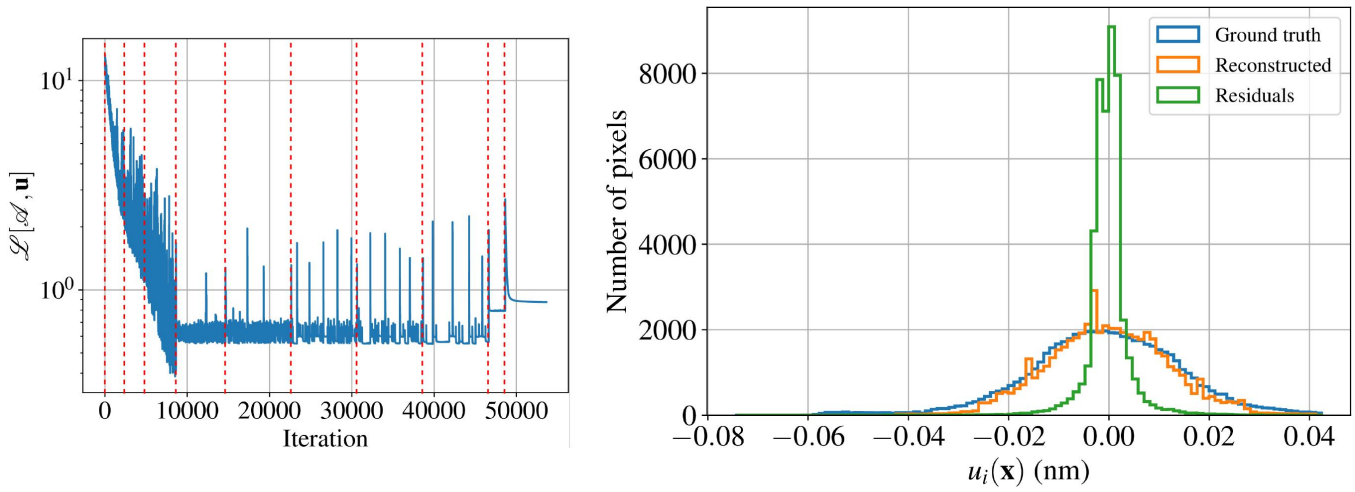

(a) **(b)**

Supplementary Figure 4: Optimization metrics for the MR-BCDI reconstruction of a simulated crystal with dislocations. **(a)** Trend in multi-reflection loss function given by Equation 3 in the main text as a function of Adam optimizer iteration (initial learning rate = 0.02) The red lines denote the beginning of a new optimization epoch. **(b)** Histogram of the simulated and reconstructed components of the vector $\boldsymbol{u}(\boldsymbol{x})$, along with point-to-point residuals of each vector component.

3 Fourier transform-based resampling

Here we describe and derive the methods of Fourier-based resampling we used to implement the T_i operation in the forward model described in the main text.

We start with the discrete object $\psi(s_0\boldsymbol{m})$, which denotes the object $\psi(\boldsymbol{x})$ sampled along the orthogonal directions $[\hat{\boldsymbol{k}}_1\ \hat{\boldsymbol{k}}_2\ \hat{\boldsymbol{k}}_3]$ of the detector frame, in steps of size s_0. Here, $\boldsymbol{m}$ is as defined in Equation 1 in the main text. We assume the digitized scatterer to be inside a cubic array of size $N \times N \times N$ pixels for simplicity. In the MR-BCDI problem, this is one of i mounting configurations (views of the sample with respect to the detector) corresponding to a single Bragg condition. We now describe the basic operations of (i) bulk deformation, (ii) shear deformation, and (iii) rigid-body rotation of the sampling grid that we use in different combinations to implement the operation T_i and that are based on established signal processing methods [5, 6, 7].

The basis matrix $\boldsymbol{B}_{\text{real}}$ for this demonstrative configuration is based on an actual BCDI measurement described in Ref. [1]:

$$\boldsymbol{B}_{\text{real}} = \begin{bmatrix} 12.72 & 0 & 0 \\ 0 & 12.72 & 0 \\ 3.21 & 2.70 & 11.87 \end{bmatrix} \text{ nm} \tag{13}$$

The resampling method $\psi(s_0\boldsymbol{m}) \to \psi(\boldsymbol{B}_{\text{real}}\boldsymbol{m})$ consists of two interpolation operations acting on $\psi(s_0\boldsymbol{m})$, performed in order: (i) 'bulk' resampling along the orthogonal directions in *new* steps of B_{11}, B_{22} and B_{33}, where B_{ii} denote the diagonal elements of $\boldsymbol{B}_{\text{real}}$, followed by (ii) a 'shear' resampling into each of the three independent orthogonal directions, corresponding to the off-diagonal elements of $\boldsymbol{B}_{\text{real}}$. We introduce for simplicity $\mathcal{F}_i$ as the 1-D Fourier transform along the axis i (where $i = 1, 2, 3$).

Further, we assign $s_0 = (\det \boldsymbol{B}_{\text{real}})^{1/3} = 12.43$ nm. This choice allows us to demonstrate both bulk stretching and compression, since is it greater than one of the B_{ii} but less than the other two. For an MR-BCDI experiment, s_0 is the user-defined size of the reconstruction grid within the bounding box $\mathcal{V}$.

3.1 Bulk resampling

Real-space resampling along the orthogonal array axes of $\psi(s_0\boldsymbol{m})$ is achieved by truncating or padding the numerical array in Fourier space. To this end, we define operations $\mathcal{P}$ and $\mathcal{T}$ that symmetrically pad or truncate the input array along the specified axis:

- $\mathcal{P}(\hat{\boldsymbol{k}}_i, n)\psi_{\boldsymbol{m}}$ denotes the operator $\mathcal{P}$ acting on an array $\psi_{\boldsymbol{m}}$ that returns an array zero-padded on either side by n pixels. This results in $2n$ more pixels along the $\hat{\boldsymbol{k}}_i$ axis.
- $\mathcal{T}(\hat{\boldsymbol{k}}_i, n)\psi_{\boldsymbol{m}}$ denotes the operator $\mathcal{T}$ acting on an array $\psi_{\boldsymbol{m}}$ that returns an array truncated/clipped on either side by n pixels. This results in $2n$ fewer pixels along the $\hat{\boldsymbol{k}}_i$ axis.

We seek to resample the real-space object array $\psi_{\boldsymbol{m}}$ along axis $\hat{\boldsymbol{k}}_i$ in steps of B_{ii} (different from the original sampling steps size s_0). The number n of pixels by which to zero-pad/truncate is easily computed from the relation between the real-space step size and the Fourier-space numerical aperture: $s_0 \propto 1/N$. If $N_i^{(\text{new})}$ is the number of pixels along $\hat{\boldsymbol{k}}_i$ after zero-padding/truncation, then we have:

$$N_i^{(\text{new})} = \left(\frac{s_0}{B_{ii}}\right) N_i \tag{14}$$

$$\implies n = \frac{1}{2}\left|N_i^{(\text{new})} - N\right| = \frac{1}{2}\left|N\left(1 - \frac{s_0}{B_{ii}}\right)\right| \tag{15}$$

Here $|\cdot|$ denotes the absolute value and the factor $1/2$ comes from the requirement to pad/truncate symmetrically. Armed with this notation, the resampling operator $\mathcal{B}(\hat{\boldsymbol{k}}_i\,|s_0 \to B_{ii}\,)$ is given by the following sequence of operations:

$$\mathcal{B}(\hat{\boldsymbol{k}}_i\,|s_0 \to B_{ii}\,) = \begin{cases} \mathcal{T}\left(\hat{\boldsymbol{k}}_i, n\right)\mathcal{F}_i^{-1}\mathcal{P}\left(\hat{\boldsymbol{k}}_i, n\right)\mathcal{F}_i & \text{if} \quad B_{ii} < s_0 \\ \mathcal{P}\left(\hat{\boldsymbol{k}}_i, n\right)\mathcal{F}_i^{-1}\mathcal{T}\left(\hat{\boldsymbol{k}}_i, n\right)\mathcal{F}_i & \text{if} \quad B_{ii} > s_0 \end{cases} \tag{16}$$

The bulk-resampled array is denoted as: $\psi'_{\boldsymbol{m}} = \mathcal{B}(\hat{\boldsymbol{k}}_i\,|s_0 \to B_{ii}\,)\psi_{\boldsymbol{m}}$. The value of n in Supplementary Equation (16) is computed from Supplementary Equation (15), in practice rounded to the nearest integer. The final, bulk-resampled object along all three orthogonal axes is given by:

$$\begin{aligned} \psi'_{\boldsymbol{m}} &\equiv \psi([B_{11}\ B_{22}\ B_{33}]^T \odot \boldsymbol{m}) \\ &= \underbrace{\mathcal{B}(\hat{\boldsymbol{k}}_1\,|s_0 \to B_{11}\,)\mathcal{B}(\hat{\boldsymbol{k}}_2\,|s_0 \to B_{22}\,)\mathcal{B}(\hat{\boldsymbol{k}}_3\,|s_0 \to B_{33}\,)}_{\text{total bulk resampling operator}}\psi_{\boldsymbol{m}} \end{aligned} \tag{17}$$

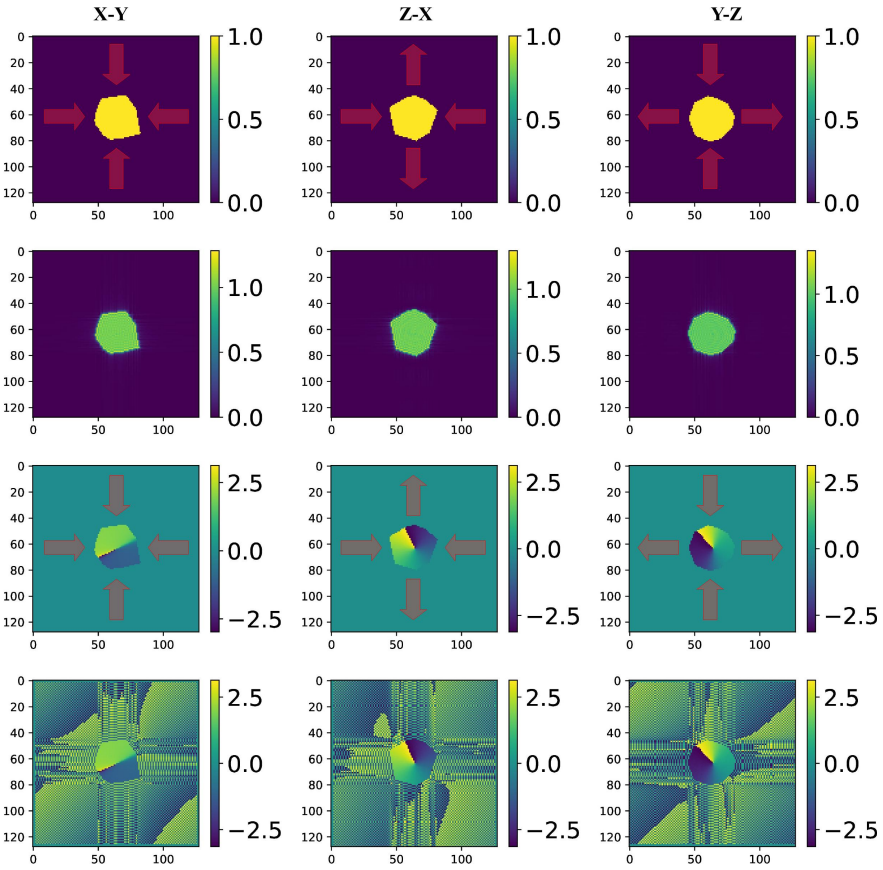

Supplementary Figure 5: Fourier transform -based bulk resampling demonstrated on a synthetic crystalline volume with a screw dislocation, marked by a winding phase at the dislocation core. **Row 1**: orthogonal slices through center of the amplitude profile of the original crystal. The arrows denote the bulk compression/expansion along the principal axes with respect to the original object, as a result of resampling. **Row 2**: central cross-sections of the resampled amplitude. **Row 3**: corresponding slices of the original phase, with the screw dislocation indicated by the phase discontinuity. **Row 4**: resampled phase profile. The plots show phase in radians.

Here $\odot$ denotes the element-wise (Hadamard) product. Bulk resampling of a synthetic object originally sampled in steps of s_0 is shown in Supplementary Figure 5. The first two rows show the amplitudes of the original and bulk-resampled object. The third and fourth rows show the corresponding complex phases. The winding phase profile is indicative of a screw dislocation passing through the center of the crystalline bulk (third row). Further, there is little difference in the sizes of the original and resampled objects because of the proximity of each B_{ii} to the chosen value of s_0. For demonstrative purposes, the fidelity of the bulk-resampling procedure to high-frequency phase features even with greatly exaggerated under/over-sampling steps is shown in Supplementary Figure 6.

We note the following:

1. The concept of upsampling with the padding operator $\mathcal{P}$ has been explored in the context of image registration [8].

2. The operator $\mathcal{B}$ in Supplementary Equation (16) returns a new array of size $N \times N \times N$ pixels which contains the original object resampled along axis i by a factor B_{ii}/s_0.

3. The upsampling enabled by Supplementary Equation (16) when $B_{ii} < s_0$ does not actually result in better sampling of any sub-pixel features in the physical object. The smallest feature dictated by the available Fourier content is merely sampled more finely. This is owing to the fact that no new Fourier information was added in the process. However, on truncation ($B_{ii} > s_0$), high-frequency information in Fourier space is truly discarded. As expected, the downsampling operation results in a loss of spatial resolution.

4. While truncation and zero-padding are not differentiable operations by themselves, *every pixel value* in the output array $\psi'_{\boldsymbol{m}}$ is still related analytically to the pixels in $\psi_{\boldsymbol{m}}$ through the Fourier transform. In the MR-BCDI problem, this analytical dependency extends back to the original unknowns, namely $A_{\boldsymbol{m}}$ and $\boldsymbol{u}_{\boldsymbol{m}}$ through multiplication and exponentiation, as well as forward to each of the inferred diffraction patterns $\left\|\Psi^{(i)}_{\boldsymbol{m}}\right\|^2$ and the loss function in Equation 3 in the main text itself. Multiplication, exponentiation and the Fourier transform

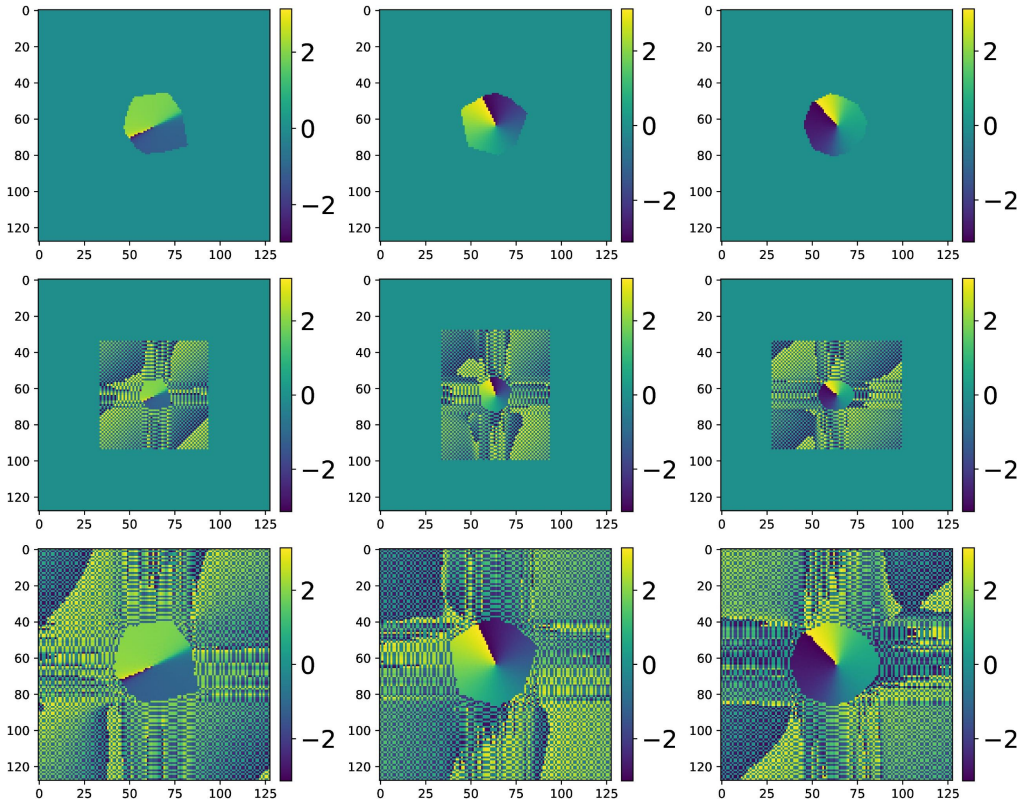

Supplementary Figure 6: Orthogonal cross sections of a discontinuous 3D phase object subjected to uniform bulk transformation $\mathcal{B}(\hat{\boldsymbol{k}}_i\,|s_0 \to \xi B_{ii}\,)$. For simplicity, $s_0 = B_{ii} = 1$ for all $i = 1, 2, 3$ (along all three axes), with (**top row**) $\xi = 1$ (original), **(middle row)** $\xi = 1.5$ and (**bottom row**) $\xi = 0.75$.

are all differentiable operations and have highly optimized implementations in modern auto-differentiation software. In the language of auto-differentiation, the computational graph is unbroken from $\mathcal{A}_{\boldsymbol{m}}$ and $\boldsymbol{u}_{\boldsymbol{m}}$ to $\mathcal{L}_{\text{multi}}$, even in the presence of a "destructive" operation like truncation. Therefore this formulation lends itself easily to auto-differentiation.

5. The $\mathcal{B}$ operators in Supplementary Equation (17) commute with each other since the resampling along each of the three axes are independent operations.

3.2 Shear resampling

The bulk resampling method described in Section. 3.1 was achieved with non-analytical operations such as zero-padding and truncation, which nevertheless connect the unknowns A and $\boldsymbol{u}$ analytically to the inferred signal. In contrast, the shear transformations corresponding to the off-diagonal elements of $\boldsymbol{B}_{\text{real}}$ are truly differentiable in nature. As we show in this subsection, they can be achieved through a combination of 1-D FTs and phase ramps. The 2D shear of a general 3D function $\xi(\boldsymbol{x}) \equiv \xi(x, y, z)$ in the yz-plane is given by the following sequence of operations:

$$\xi(x + \alpha y + \beta z, y, z) = \underbrace{\int_{\mathbb{R}} dk\; e^{\iota 2\pi k x}}_{\mathcal{F}_1^{-1}} \underbrace{e^{\iota 2\pi k(\alpha y + \beta z)}}_{\text{phase shift}} \underbrace{\int_{\mathbb{R}} dx\; e^{-\iota 2\pi k x}\, \xi(x, y, z)}_{\mathcal{F}_1} \tag{18}$$

$$= \underbrace{\mathcal{F}_1^{-1} \Phi_{23}(k\,|\alpha, \beta\,) \mathcal{F}_1}_{\text{off-diagonal shear}} \xi(x, y, z) \tag{19}$$

Here, $\Phi_{23}(k\,|\alpha, \beta\,) \equiv \exp[\iota 2\pi k(\alpha y + \beta z)]$ is the phase ramp applied to axes 2 and 3 (in this case, y and z respectively). Similar phase ramps $\Phi_{31}(k|\alpha, \beta)$ and $\Phi_{12}(k|\alpha, \beta)$ are constructed with the 1D Fourier transforms $\mathcal{F}_2$ and $\mathcal{F}_3$ to achieve shears along the zx- and xy-planes. These are given by:

$$\Phi_{31}(k|\alpha, \beta) = \exp[\iota 2\pi(\alpha z + \beta x)] \tag{20}$$

$$\Phi_{12}(k|\alpha, \beta) = \exp[\iota 2\pi(\alpha x + \beta y)] \tag{21}$$

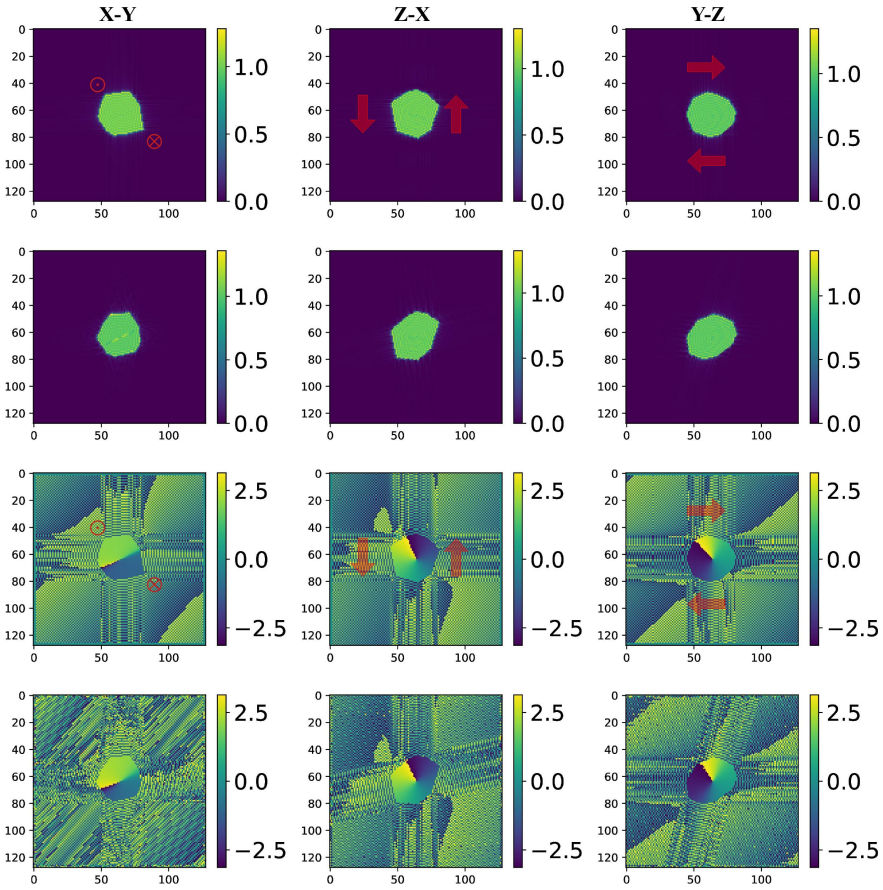

Supplementary Figure 7: **Row 1**: amplitude cross-section of the *bulk-resampled* digital object in Supplementary Figure 5, before application of the shearing operator in Supplementary Equation (23). The arrows denote the direction of shearing. The $\otimes$ and $\odot$ symbols denote arrows entering and exiting the plane of the figure respectively. **Row 2**: shear-resampled object amplitude cross-sections. **Row 3,4**: corresponding phase profiles, indicating the screw dislocation. All phase plots are in radians.

The use of the sampling matrix $\boldsymbol{B}_{\text{real}}$ from Ref. [1] lends itself easily to the compact formulation of the shear operator in Supplementary Equation (19). To see this, we consider the desired sampling step along $\hat{\boldsymbol{k}}_1$, namely $B_{11}l + B_{12}m + B_{13}n$ (where $\boldsymbol{m} \equiv [l\ m\ n]^T \in \mathbb{Z}^3$). This may be obtained from $\psi'_{\boldsymbol{m}}$ in Supplementary Equation (17) by:

$$\begin{aligned}\psi''_{\boldsymbol{m}} \equiv \psi'([B_{11}\ B_{22}\ B_{33}]^T\boldsymbol{m}) \longrightarrow \\ \psi'([B_{11}l + B_{12}m + B_{13}n\ B_{22}\ B_{33}]^T\boldsymbol{m}) \\ = \underbrace{\left[\mathcal{F}_1^{-1}\Phi_{23}\left(k\left|\frac{B_{12}}{B_{11}}, \frac{B_{13}}{B_{11}}\right.\right)\mathcal{F}_1\right]}_{yz\text{ shear operator}}\psi'_{\boldsymbol{m}}\end{aligned} \tag{22}$$

where the yz-shear operator acts not on the original objet $\psi(s_0\boldsymbol{m})$, but the *bulk-resampled* object $\psi'_{\boldsymbol{m}}$ from Supplementary Equation (17). Consequently, the complete shear operation is given by the composition of the shear operators along the independent Cartesian directions:

$$\begin{aligned}\psi''_{\boldsymbol{m}} &\equiv \psi(\boldsymbol{B}_{\text{real}}\boldsymbol{m}) \\ &= \left[\mathcal{F}_3^{-1}\Phi_{12}\left(k\left|\frac{B_{31}}{B_{33}}, \frac{B_{32}}{B_{33}}\right.\right)\mathcal{F}_3\right] \circ \left[\mathcal{F}_2^{-1}\Phi_{31}\left(k\left|\frac{B_{23}}{B_{22}}, \frac{B_{21}}{B_{22}}\right.\right)\mathcal{F}_2\right] \circ \left[\mathcal{F}_1^{-1}\Phi_{23}\left(k\left|\frac{B_{12}}{B_{11}}, \frac{B_{13}}{B_{11}}\right.\right)\mathcal{F}_1\right]\psi'_{\boldsymbol{m}}\end{aligned} \tag{23}$$

where $\circ$ denotes operator composition. Supplementary Figure 7 shows the effect of the shear resampling operation in Supplementary Equation (23) applied to the bulk-resampled object (Supplementary Figure 5, row 2). Once again we note the fidelity to the original discontinuity, which would have not been possible with a simple real-space interpolation within the space of a single voxel.

Supplementary Equation (17) and Supplementary Equation (23) together denote the sequence of analytic operations that take the unknown object $\psi(s_0\boldsymbol{m})$ to the appropriately sampled object $\psi(\boldsymbol{B}_{\text{real}}\boldsymbol{m})$, for direct use in

Equation 3 in the main text. The complete resampling operation $\psi(s_0\boldsymbol{m}) \longrightarrow \psi(\boldsymbol{B}_{\text{real}}\boldsymbol{m})$ *differentiably* transforms the original object (Supplementary Figure 5, row 1) to the appropriately resampled object (Supplementary Figure 7, row 2), while preserving the fidelity to high-frequency features within the object (in this case, phase discontinuities).

3.3 Resampling by grid rotation

Building upon the shear-resampling methodology in Section 3.2, we describe our last fundamental resampling operation in which the discrete grid of the object is arbitrarily rotated. This is of crucial importance in the MR-BCDI problem, since the scatterer has to be rotated into different Bragg conditions in turn. The method decomposes the desired rotation into a sequence of shear operations, and therefore has all the advantages of the shear-resampling method, including differentiability and maximum fidelity to small features.

As an example, we wish to actively rotate the discretized object $\psi(s_0\boldsymbol{m})$ by an angle θ about the axis $+\hat{\boldsymbol{k}}_3$ (in a right-handed manner). Practically, we rotate the Cartesian sampling grid by $-\theta$ about $+\hat{\boldsymbol{k}}_3$. According to Refs. [5, 6, 7], Supplementary Equation (19) may be employed to achieve this by three successive shear operations:

$$\begin{aligned}\mathcal{R}(\theta,\hat{\boldsymbol{k}}_3)\psi(\boldsymbol{x}) &\equiv \psi\left(x\cos\theta + y\sin\theta, -x\sin\theta + y\cos\theta, z\right)\\ &= \left[\mathcal{F}_1^{-1}\Phi_{12}\left(k\,\middle|0,\tan\frac{\theta}{2}\right)\mathcal{F}_1\right]\circ\left[\mathcal{F}_2^{-1}\Phi_{12}\left(k\,|-\sin\theta,0\right)\mathcal{F}_2\right]\circ\left[\mathcal{F}_1^{-1}\Phi_{12}\left(k\,\middle|0,\tan\frac{\theta}{2}\right)\mathcal{F}_1\right]\psi(\boldsymbol{x})\end{aligned} \quad (24)$$

Similar formulations to Supplementary Equation (24) hold for rotations $\mathcal{R}(\theta,\hat{\boldsymbol{k}}_1)$ and $\mathcal{R}(\theta,\hat{\boldsymbol{k}}_2)$ about the $\hat{\boldsymbol{k}}_1$ and $\hat{\boldsymbol{k}}_2$ directions. Using this method, we can express the grid resampling of an *arbitrary* rotation $\mathcal{R}(\theta,\hat{\boldsymbol{n}})$ as a composition of three rotations:

$$\mathcal{R}(\theta,\hat{\boldsymbol{n}}) = \mathcal{R}(\alpha_3,\hat{\boldsymbol{k}}_3)\circ\mathcal{R}(\alpha_2,\hat{\boldsymbol{k}}_2)\circ\mathcal{R}(\alpha_1,\hat{\boldsymbol{k}}_1) \quad (25)$$

Here the α_i denote the Euler angles of rotation in the XYZ convention (*i.e.*, rotation about X followed by Y and then Z). We note that regardless of the Euler convention, an arbitrary rotation may be achieved by a triplet of successive rotations about the principal Cartesian axes.

The rotation of the example crystal from the previous examples by an angle of 45° about the Y-axis is shown in Supplementary Figure 8. Again we note the fidelity the resampled object to the discontinuity in the bulk. Supplementary Figure 9 contains an example that contrasts Fourier-based rotation resampling with regular grid interpolation in a crystal containing multiple phase discontinuities.

We note here in our global optimization scheme, $\mathcal{A}$ and $\boldsymbol{u}$ are defined and reconstructed only within an estimated bounding box $\mathcal{V}$ of the object. However, the transformations described in this section are applied to a zero-padded version of $\mathcal{V}$. In this paper, all buffered arrays are of size $128\times128\times128$. While our interpolation approach ensures that phase discontinuities are well-preserved, we note that object amplitude suffers from oscillations at sharp edges and discontinuities arising from the Gibbs phenomenon. This is evident on comparing the first and second rows in Supplementary Figures 5 and 7. However, this problem is automatically addressed in our global optimization scheme through the use of the total-variation (TV) regularizer. As we have shown, this results in oscillation-free edges in the electron density reconstructions.

Further, we note that a large rotation angle about a principal axis (for example, θ about the Z-axis from Supplementary Equation (24)), when implemented with the fast Fourier transform, potentially causes the transformed object to be split across the periodic array boundary, due to an excessively large shear. Whether or not this splitting takes place depends on the size of θ and the ratio of the crystal-to-buffer sizes in each array dimension. A smaller ratio implies a larger θ can be accommodated before splitting commences. This undesirable effect can be addressed by performing a large principal rotation in a sequence of smaller rotations. In this work, we have conservatively set this smaller rotation size to 45°. With this convention, a rotation of 210° about the Z-axis would be decomposed as four rotations of 45° followed by a 30° rotation. While this certainly lengthens the chain of analytic computations for each optimization step, we have found this to introduce negligible overhead when implemented on the GPU.

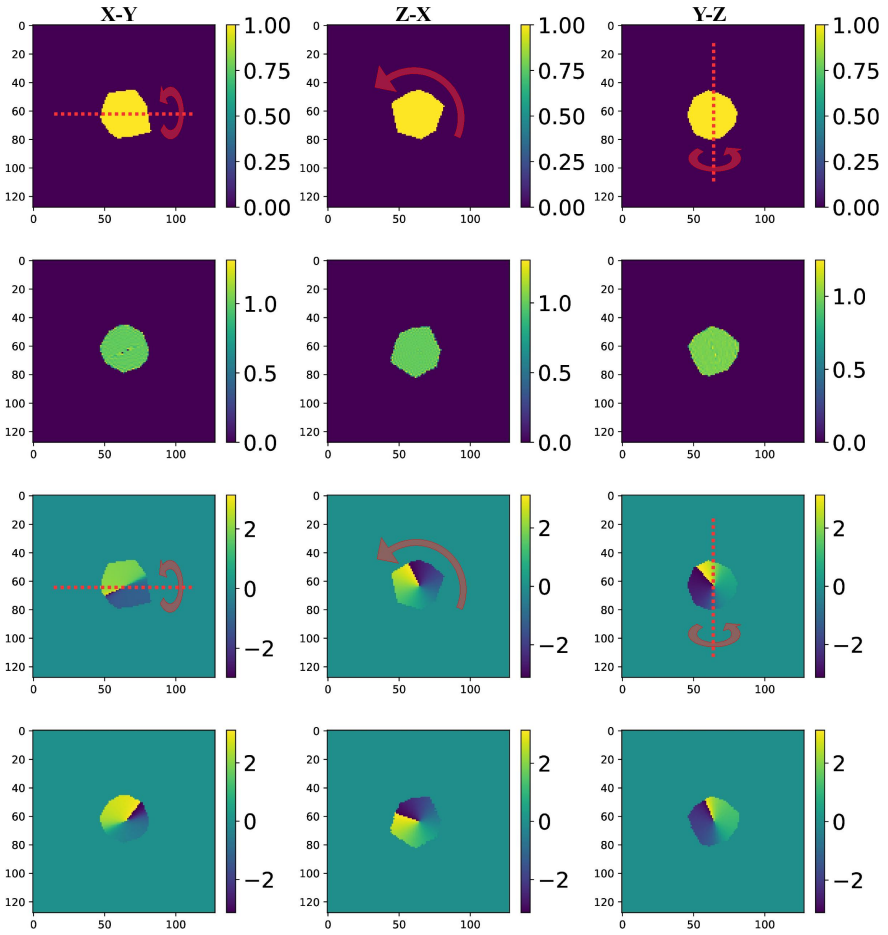

Supplementary Figure 8: **Row 1**: Mutually orthogonal cross sections of the original scatterer amplitude. The arrows indicate the direction of the 45° rotation about the Y-axis viewed from different perspectives. **Row 2**: scatterer amplitude after it has been rotated within the grid. **Row 3, 4**: corresponding complex phase cross sections. All phase plots are in radians.

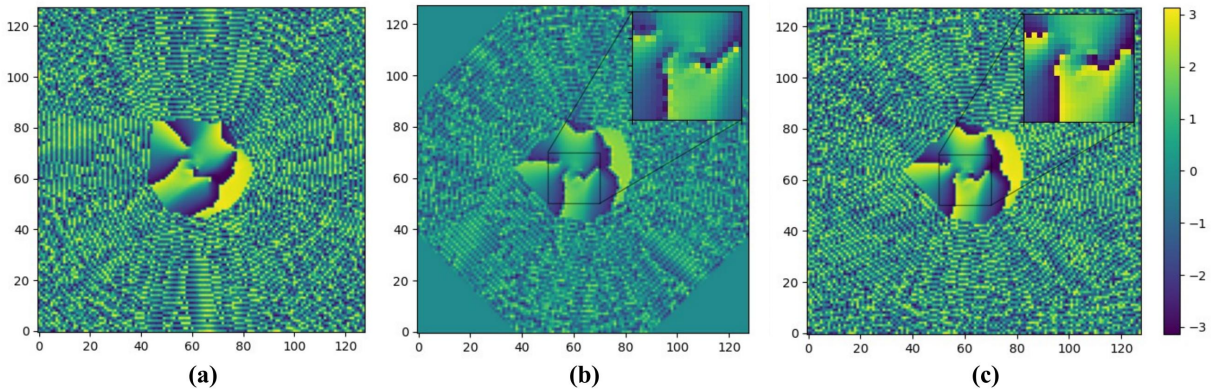

Supplementary Figure 9: **(a)** 2D slice of 3D discontinuous phase object prior to resampling by grid rotation. **(b)** Grid rotation by simple multi-linear interpolation between neighboring voxels. **(c)** Grid rotation by Fourier transform -based interpolation (Supplementary Equation (24)). The inset plots highlight the difference in fidelity to small, pixel-scale features.

4 Constraining displacement field magnitude

In Section 2.3.1 in the main text we noted that we restricted $\boldsymbol{u}(\boldsymbol{x})$ to lie within the lattice plane spacings defined by the [100], [010] and [001] directions of the crystal. This constraint is not a loss of generality when we consider the conditions under which phase wrapping takes place for a particular Bragg reflection. The phase at a point $\boldsymbol{x}$ corresponding to a reflection $\boldsymbol{G}_{hkl}$ is given by: $\phi(\boldsymbol{x}) \equiv 2\pi \boldsymbol{G}_{hkl} \cdot \boldsymbol{u}(\boldsymbol{x})$. Therefore a phase wrap is associated with an excess displacement $\boldsymbol{d}_{hkl}$ given by: $\phi(\boldsymbol{x}) + 2m\pi = 2\pi \boldsymbol{G}_{hkl} \cdot [\boldsymbol{u}(\boldsymbol{x}) + m\boldsymbol{d}_{hkl}]$, where $m \in \mathbb{Z}$. Here, $\boldsymbol{d}_{hkl}$ is the vector in the direction of $\boldsymbol{G}_{hkl}$ and whose magnitude is equal to the hkl lattice plane spacing, with $\|\boldsymbol{G}_{hkl} \cdot \boldsymbol{d}_{hkl}\| = 1$ in crystallographers' units. We see that for a given $\boldsymbol{G}_{hkl}$, $\boldsymbol{u}(\boldsymbol{x})$ is determined up to an integer multiple of $\boldsymbol{d}_{hkl}$ in the same sense that the phase is only determined up to an integer multiple of 2π. We therefore deduce that any $\boldsymbol{u}(\boldsymbol{x})$ may be reduced to a 'fundamental zone' between the parallel lattice planes located at $\boldsymbol{u}(\boldsymbol{x}) = \boldsymbol{0}$ and $\boldsymbol{u}(\boldsymbol{x}) = \boldsymbol{d}_{hkl}$ (or equivalently, $\pm\boldsymbol{d}_{hkl}/2$), by addition or subtraction of an appropriate number of $\boldsymbol{d}_{hkl}$ [9]. The reduced $\boldsymbol{u}(\boldsymbol{x})$ is guaranteed to generate the same phase in the outgoing object wave. Thus, as a purely computational convenience, we constrain $\boldsymbol{u}(\boldsymbol{x})$ at each point to lie within the intersection of the three largest 'fundamental zones' of the crystal lattice, which correspond to the lattice plane separations along the lowest-index directions (*i.e.*, $\|\boldsymbol{d}_{100}\|$, $\|\boldsymbol{d}_{010}\|$ and $\|\boldsymbol{d}_{001}\|$). This volume of intersection is rectangular for a cubic or orthorhombic crystal, but in general is a sheared parallelopiped. An instance of utilizing this constraint with such a crystal was presented in the main text for the SiC nanocrystal in which the $[10\bar{1}0]$, $[01\bar{1}0]$ and [0001] are non-orthogonal and the last two directions are separated by 120°. This constraint on $\boldsymbol{u}(\boldsymbol{x})$ primarily serves to prevent spurious discontinuities in the reconstructed $\boldsymbol{u}(\boldsymbol{x})$ resulting from excessively large gradient descent steps, which could cause the $\boldsymbol{u}(\boldsymbol{x})$ at adjacent voxels to converge to different but phase-equivalent values.

References

[1] S. Maddali, P. Li, A. Pateras, D. Timbie, N. Delegan, A. L. Crook, H. Lee, I. Calvo-Almazan, D. Sheyfer, W. Cha, F. J. Heremans, D. D. Awschalom, V. Chamard, M. Allain, and S. O. Hruszkewycz. General approaches for shear-correcting coordinate transformations in Bragg coherent diffraction imaging. Part I. *Journal of Applied Crystallography*, 53(2), Apr 2020.

[2] P. Li, S. Maddali, A. Pateras, I. Calvo-Almazan, S.O. Hruszkewycz, W. Cha, V. Chamard, and M. Allain. General approaches for shear-correcting coordinate transformations in Bragg coherent diffraction imaging. Part II. *Journal of Applied Crystallography*, 53(2), Apr 2020.

[3] S. Maddali. *Phaser*: Python-based bcdi phase retrieval for cpu and gpu (github), 2020.

[4] S. Marchesini. Invited article: A unified evaluation of iterative projection algorithms for phase retrieval. *Review of Scientific Instruments*, 78(1):011301, 2007.

[5] Michael Unser, Philippe Thevenaz, and Leonid Yaroslavsky. Convolution-based interpolation for fast, high-quality rotation of images. *IEEE Transactions on image processing*, 4(10):1371–1381, 1995.

[6] Kieran G Larkin, Michael A Oldfield, and Hanno Klemm. Fast fourier method for the accurate rotation of sampled images. *Optics communications*, 139(1-3):99–106, 1997.

[7] Philippe Thévenaz, Thierry Blu, and Michael Unser. Interpolation revisited [medical images application]. *IEEE Transactions on medical imaging*, 19(7):739–758, 2000.

[8] Manuel Guizar-Sicairos, Samuel T. Thurman, and James R. Fienup. Efficient subpixel image registration algorithms. *Opt. Lett.*, 33(2):156–158, Jan 2008.

[9] Kandel, Saugat. *Using automatic differentiation for coherent diffractive imaging applications.* PhD thesis, 2021.